Design of high-efficiency resonant-cavity-enhanced GeSn single-photon avalanche photodiodes for optical quantum and sensing applications

Qimiao Chen*, Shaoteng Wu, Lin Zhang, Weijun Fan *Member, IEEE* and Chuan Seng Tan*, *Senior Member, IEEE*

***Abstract*— A novel resonant-cavity-enhanced (RCE) GeSn single-photon avalanche photodiode (SPAD) detector is proposed and optimized for high-efficiency single-photon detection at 1,550 and 2,000 nm wavelength at room temperature for sensing and optical quantum applications. The corresponding fabrication methods based on direct epitaxy and wafer bonding are proposed as well. The RCE GeSn SPAD consists of a PIPIN GeSn/Si heterostructures embedded in an optical cavity form by a distributed Bragg reflector (DBR) and GeSn surface. The results show that high photon absorption efficiency and avalanche triggering probabilities can be achieved by careful design of DBR reflectors, GeSn absorber, doping concentrations of Si charge sheet layer and multiplication layer, which lead to a high single-photon detection efficiency (SPDE) of ~80%, which is promising for emerging quantum applications demanding high SPDE, such as linear optical quantum computing. The noise equivalent power (NEP) and dark count rate (DCR) as a function of threading dislocations density (TDD) are examined as well. It is found that the device could operate near room temperature with a similar DCR level to that of Ge SPAD operating at low temperature . A NEP of ~3x10^{15} W/Hz$^{1/2}$ is observed from RCE GeSn SPAD for 1,550 nm wavelength at room temperature. This work shows that the proposed RCE GeSn SPADs are promising candidates for high-efficiency single-photon detection in short-wave infrared (SWIR) regime for sensing and optical quantum applications**

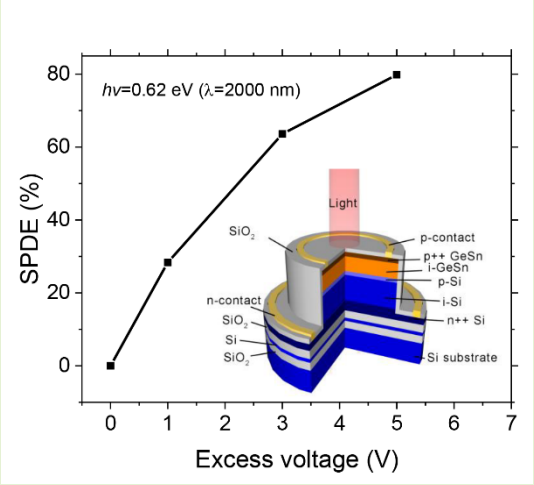

***Index Terms*— Resonant cavity, GeSn alloys, single-photon avalanche diode photodetector, short-wave infrared.**

I. Introduction

A single-photon detector (SPD), which has the capability of single-photon detection, has been widely used during the past two decades in numerous applications, including quantum computing [1], quantum communication [2], [3], Light Detection And Ranging (LIDAR) [4] and fluorescence medical imaging [5]. At present, there are several SPDs available, including photomultiplier tubes, superconducting SPDs [6]–[8] and semiconductor single-photon avalanche diodes (SPADs) [9]–[13]. Photomultiplier tubes have large active areas, but they suffer from high dark count rate (DCR) and low single-photon detection efficiency (SPDE). Superconducting SPDs can provide high SPDE as well as low DCR. However, the extremely low operating temperature (cryogenic temperature, typically below 4 K) of them limits their practical applications. Currently, SPAD is a more practical approach for single-photon detections, which is biased above its reverse-bias breakdown voltage, resulting in a self-sustaining avalanche that enables responses to even a single photon absorption. For wavelength below 1000 nm, Si SPADs have demonstrated excellent performance and been used in a wide range of sensing and quantum photonic applications [2]–[4]. However, there exists a strong demand for extending the wavelength range into short-wave infrared (SWIR, typically defined as the wavelength range of 1100~2500 nm), which is beyond the detection coverage of Si SPAD. Firstly, the 1550 nm wavelength is the optical fibre telecommunications window and SPADs at 1550 nm will benefit numerous fibre-based applications. Furthermore, the 2000 nm low-loss hollow-core photonic band gap (HC-PBG) fibre window is a promising window for the next generation telecommunication [14]. The compatibility with the 2000 nm window will be strategic for future applications. Secondly, the eye-safety thresholds for SWIR is higher than that of visible and NIR region in free-space applications [15]. The atmospheric attenuation of SWIR bands is lower than that of the visible and NIR bands [16]. Finally, the background noise of single-photon LIDAR system due to solar

The authors are with School of Electrical and Electronic Engineering, Nanyang Technological University, 50 Nanyang Avenue, 639798 Singapore (e-mail: chenqm@ntu.edu.sg; tancs@ntu.edu.sg)

radiation decreases considerably in the SWIR regime [17].

In the SWIR regime, the development of a high-performance SPAD, however, is challenging. InGaAs/InP SPAD detectors are most widely used in the SWIR regime with detection wavelengths up to 1600 nm and operating temperature between 220 and 255 K [18]–[20]. However, the group III-V SPAD detectors are not compatible with current Si CMOS processing. Besides, the after pulsing effect, where carriers trapped in the defect levels are emitted after the detection to trigger new avalanches events, also limits the count rates of the SPADs. Alternatively, Group IV material, Ge, is a candidate that can cover detection wavelengths up to 1550 nm at room temperature and is CMOS compatible. Ge/Si SPADs with different structures have been reported, such as mesa geometry normal incidence Ge/Si SPADs [21], [22], waveguide Ge/Si SPADs [12] and planar Ge/Si SPADs [13]. The waveguide Ge/Si SPAD demonstrated an SPDE of 5.27% at a wavelength of 1310 nm with an operating temperature of 80 K. The state-of-the-art Ge SPAD is the planar Ge-on-Si SPADs, demonstrating an SPDE of 38% and a noise-equivalent power (NEP) of $2x10^{-16}$ $WHz^{-1/2}$ at 125 K at 1310 nm wavelength, which compares more favorably with commercial InGaAs/InP SPADs. Although promising, Ge-on-Si SPADs suffer from some issues. Firstly, the absorption coefficient of Ge at 1550 nm operating wavelength is low and insufficient for absorbing photons. For the demonstrated Ge SPAD, detection wavelength cutoff even reduced below 1550 nm at low temperature due to the enlarged bandgap by the decreased operating temperature. Besides, due to the low absorption coefficient, the thickness of Ge absorbers has to be greater than 1 μm so as to achieve an efficient absorption. However, the thick Ge will increase the noise (DCR) and decrease the photon timing performance (jittering time). Therefore, it is more preferred to improve the sensitivity of SPAD with a thin absorption layer. Secondly, Ge can hardly cover the wavelength beyond 1600 nm.

Here, we propose a novel SPAD structure of resonant-cavity-enhanced (RCE) GeSn-based SPAD to realize high-performance single-photon detection in the SWIR regime for sensing and optical quantum applications. The proposed device has the following innovations and advantages over the state-of-the-art Ge-on-Si and InGaAs/InP SPADs: (i) Coupling with a vertical optical cavity to enhance the absorption efficiency (approaches 100%) with a thin absorption layer, resulting in high detection efficiency and low noise of the SPAD. (ii) High absorption coefficient (can achieve > 10000 cm^{-1}) at 1550 nm and 2000 nm, resulting in high detection efficiency. (iii) Broad detection wavelength coverage up to 2500 nm. (iv) Compatibility with Si-CMOS technology and easy to be scaled down and integrated with electronic devices, leading to low costs.

This paper is structured as follows: The proposed device architecture and corresponding fabrication methods are presented in section II; Theoretical models for device design and performance prediction are described in section III; Results are analyzed and discussed in section IV, and conclusions are summarized in section V finally.

II. Design and Proposed Fabrication Flow of GeSn RCE-SPADs

To achieve high SPDE, low DCR and high operation temperature, several designs are made. Firstly, we select the separate absorption and carrier multiplication (SACM) structure which has been proved as an efficient approach to reduce the DCR by avoiding band-to-band tunneling in absorption layers. Photons are absorbed in GeSn layers and the photo-generated electrons drift into Si multiplication layer to trigger avalanche evens. Secondly, we sandwich the GeSn absorber and Si multiplier with a resonant cavity in which the photon absorption probability in the absorption layer will be enhanced, thus increasing the SPDE. The Sn content of GeSn will be tailored to achieve high absorption coefficients. In this work, 3% Sn concentration is chosen for the absorption at the wavelength of 1550 nm and 10% Sn concentration is chosen for the absorption at 2000 nm. Other design considerations are the electric field profile (high in Si multiplier and moderate in GeSn absorber), the doping concentration and thickness of charge sheet layer and threading dislocations density (TDD) effect.

Fig. 1 shows the schematic of the architecture of the designed RCE GeSn SPAD, which consists of a p++ GeSn, i GeSn, p Si, i Si and n++Si heterostructures layers embedded in an optical cavity form by a distributed Bragg reflector (DBR) and GeSn surface. The thickness of the DBR layers is designed specifically to obtain a high reflectance at a wavelength of 1550 nm or 2000 nm. The thickness of GeSn is designed to achieve high absorption efficiency. The thickness and doping concentration of the charge layer (p-Si layer) are optimized to obtain a proper electric field distribution in the SPAD and a high device performance. To achieve a high triggering probability of an avalanche event, a thick Si multiplication layer is chosen. Table I summarizes the thicknesses and doping profiles of the GeSn SPAD.

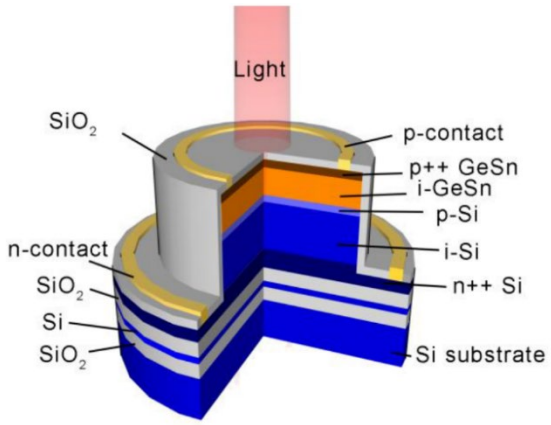

Fig. 1. Schematic of the RCE GeSn SPAD, consisting PIPIN GeSn/Si structure sandwiched by an optical cavity

TABLE I
DIMENSIONS AND DOPING CONCENTRATION OF RCE GESN SPAD

Layer	Thickness (nm)	Doping concentration (cm^{-3})
p++ GeSn contact layer	50	5×10^{19} (p)
i GeSn absorption layer	d	$1x10^{15}$ (p)
p Si charge sheet layer	50	$3x10^{17}$ (p)
i Si multiplication layer	1000	$1x10^{15}$ (p)
n++ Si contact layer	220	$1x10^{20}$ (n)

The fabrication flow of the device is proposed and shown in Fig. 2. The SPAD is grown on n++ doped silicon substrates with buried DBR fabricated by a double-SOI process [23]. Firstly, a 1050 nm Si multiplier is grown by a commercial RPCVD system. The charge sheet layer is doped by ion implantation or *in situ* doping, followed by rapid thermal annealing. Then, after cleaning, an intrinsic GeSn and a 50 nm p++ GeSn top contact layer are grown on Si charge sheet layer by RPCVD (step c-i). Alternatively, GeSn/Ge/Si wafer can be bonded to the doped double-SOI wafers by wafer bonding technique [24], followed by Si grinding, Ge CMP and ion implantation (step c-ii), which is expected to have lower TDDs than that of direct epitaxial GeSn. Then the mesa is defined by lithography and dry etching. Finally, metal contacts, passivation layers are deposited.

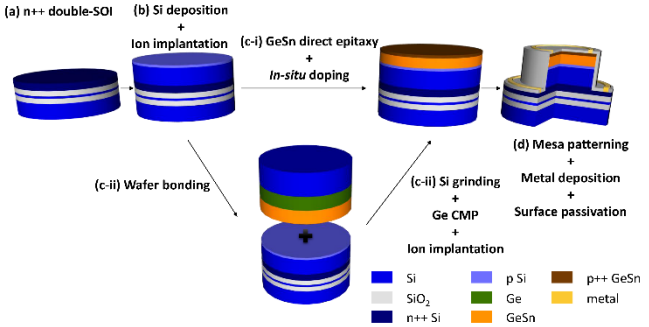

Fig. 2. 3D schematic of the proposed fabrication process of the RCE GeSn SPAD.

III. Theoretical Models

Theoretical models for the proposed GeSn RCE-SPAD are presented in this section. The modeling parameters include reflectivity of DBR, absorption efficiency, absorption coefficient, SPDE, DCRs and noise equivalent power (NEP). The parameters of GeSn alloys are calculated by linear interpolation of parameters of Ge and α-Sn except bandgaps. The bandgaps of unstrained GeSn alloy are described by quadratic polynomials including bowing parameters (b_Γ= 2.18 eV and b_L = 0.68 eV) [25].

A. Reflectivity and reflection phase of Si/SiO$_2$ DBR

Increase the absorption efficiency of GeSn within a resonant cavity will first require a DBR optimized for high reflectivity around the designed wavelength (1550 nm or 2000 nm). A transfer matrix method is utilized to calculate the reflectivity and reflection phase of the DBR considering the refractive index, wavelength and number of DBR layers. The characterized matrix for light transmitting through a single layer is given by:

$$M = \begin{bmatrix} \cos(k_0 h) & i\sin(k_0 h)/\Gamma \\ i\Gamma\sin(k_0 h) & \cos(k_0 h) \end{bmatrix} \quad (1)$$

where

$$\Gamma = \sqrt{\frac{\varepsilon_0}{\mu_0}} n\cos\theta \qquad k_0 h = nd\cos\theta \cdot 2\pi/\lambda \quad (2)$$

θ and λ are the refractive angle and the wavelength of incident light, respectively. n and d are refractive index and the thickness of the layer, respectively. Then the characterized matrix for light transmitting through multilayers can be obtained by

$$M = M_1 \times M_2 \times \cdots \times M_n = \begin{bmatrix} m_{11} & m_{12} \\ m_{21} & m_{22} \end{bmatrix} \quad (3)$$

Then the reflectivity R and reflection phase ψ can be obtained by:

$$r(\lambda) = \frac{\Gamma_0 m_{11} + \Gamma_0\Gamma_s m_{12} - m_{21} - \Gamma_s m_{22}}{\Gamma_0 m_{11} + \Gamma_0\Gamma_s m_{12} + m_{21} + \Gamma_2 m_{22}} \quad (4a)$$

$$R(\lambda) = |r(\lambda)|^2 \quad (4b)$$

$$\psi(\lambda) = -\arg[r(\lambda)] \quad (4c)$$

where subscripts s and 0 refer to the substrate and incident material, respectively

B. Single-photon detection efficiency

In SACM SPAD, SPDE is the probability that photons absorbed in the absorption layer and the photo-generated carrier quickly drifts to the multiplication layer to trigger an avalanche. The SPDE is given by [26]:

$$\mathrm{SPDE} = \eta_{abs} \times \eta_{inj} \times Pe(z_p) \quad (5)$$

where η_{abs} and η_{inj} are the absorption efficiency and the collection efficiency, respectively. $Pe(z_p)$ is the avalanche triggering probability for electrons at the location of the depletion region edge on the p-side. According to the previous study on Ge SPAD, η_{inj} is not the limiting factor of SPDE [13].

The absorption efficiency η_{abs} of the RCE SPAD is estimated by the following equation [27]:

$$\eta_{abs} = \frac{(1+R_2e^{-\alpha d})(1-R_1)(1-e^{-\alpha d})}{1-2\sqrt{R_1R_2}e^{-\alpha d}\cos(2\beta L+\psi_1+\psi_2)+R_1R_2e^{-2\alpha d}} \quad (6)$$

where R_1 and R_2 are the reflectivity values of the top and bottom mirrors, respectively. ψ_1 and ψ_2 are the reflection phase shifts introduced by the top and bottom mirrors, respectively. α, d and L are the absorption coefficient, the thickness of the GeSn layer and cavity length, respectively. The propagation constant can be obtained by $\beta=2\pi n/\lambda$. is The absorption coefficient of GeSn considering absorption from direct bandgap is given by [28]:

$$\alpha(h\nu) = \frac{A(h\nu - E_g^\Gamma)^{\frac{1}{2}}}{h\nu} \text{ for } h\nu \geq E_g^\Gamma + \frac{\Delta E}{2} \quad (7)$$

where A and $h\nu$ is the is a constant and the energy of the incident photon, respectively. E_g^Γ is the direct band gap, ΔE is the Urbach width. The absorption from indirect band gap is neglected since the absorption coefficient for indirect band gap transition is small (<100 cm^{-1}).

The triggering probabilities of electrons P_e, and holes P_h at the position z in the depletion region can be solved using the following equations [29]:

$$\frac{\partial P_e}{\partial z} = (1-P_e)\alpha_e(E)(P_e + P_h - P_eP_h) \quad (8a)$$

$$\frac{\partial P_h}{\partial z} = -(1-P_h)\alpha_h(E)(P_e + P_h - P_eP_h) \quad (8b)$$

where $\alpha_e(E)$ and $\alpha_h(E)$ are the impact ionization coefficients of electron and hole depending on the local electric field. $a_v(E) = a_v^{\infty}\, e^{-(E_v^0/E)}$ where v refers to e or h and E is the local electric field, a_v^{∞} and E_v^0 are material constants.

The electrical information of SPAD, such as the breakdown voltage, the electric field distribution can be calculated with the aid of Technology Computer Aided Design (TCAD) software *Lumerical* utilizing Poisson, drift-diffusion and continuity equations.

C. Dark count rate

For SPAD in darkness, thermally generated carriers can trigger avalanche events, which is known as the dark counts. The DCR can be evaluated by [30]:

$$\mathrm{DCR} = \mathrm{S}\int (P_e + P_h - P_eP_h)G\,\mathrm{d}z \quad (9)$$

where S is the active area of the SPAD, and G is the net generation rate of the carries. Three main generation mechanisms are responsible for the DCR of SPAD, including thermal generation and recombination (SRH), trap-assisted tunneling (TAT) and band-to-band tunneling (BTBT). According to the well-known Schockley-Read-Hall theory, the thermal generation rate of carriers considering the TAT effect and doping concentration effects is given by [31], [32]:

$$G_{SRH,TAT} = \frac{n_i}{\frac{\tau_n f}{1+\Gamma}\exp\left[\frac{-(E_t-E_i)}{kT}\right] + \frac{\tau_p f}{1+\Gamma}\exp\left[\frac{-(E_t-E_i)}{kT}\right]} \quad (10)$$

where n_i is the intrinsic carrier concentration. τ_n (τ_p) is the lifetime of electron (holes). E_i and E_t are the intrinsic Fermi level and recombination center levels, respectively. k and T are the Boltzmann constant and absolute temperature, respectively. Carrier lifetimes are related to the trapping density N_t and TDD N_{TDD}, which can be expressed by [33]:

$$\tau_{n,p} = \frac{1}{CN_{TDD}} \quad (11)$$

where C is a material parameter, which is related to trap capture cross-section, carrier thermal velocity and number of traps per unit length of dislocation. Since there is few study on GeSn, we use results for Ge photodiodes [34] to extract the parameter C, which is estimated to be 0.19 cm^2/s. Additionally, the correction term Γ accounting for the field-effect of TAT is given by Hurkx's model [35]. The correction term f accounting for doping concentration effects is given by Fossum's model [36], [37]. When the electric field is high, BTBT generation rate will be significant. The BTBT generation rate of carriers for indirect bandgap semiconductors is given by Hurkx's model [35]:

$$G_{BTBT} = B|E|^{2.5} exp\left(-\frac{E_0}{E}\right) \quad (12)$$

where B and E_0 are material parameters. Based on the simulated SPDE and DCR, NEP can be estimated as [13]:

$$NEP = \frac{h\nu}{SPDE}\sqrt{2DCR} \quad (13)$$

IV. RESULTS AND DISCUSSION

A. Optimized optical absorption efficiency of RCE GeSn SPAD at 1550 nm and 2000 nm

Fig. 3(a) and 3(b) illustrate the simulated reflectivity of DBRs with different Si/SiO_2 pairs (N) which are designed to be highly reflective at 1550 nm and 2000 nm wavelength, respectively. Since both Si and SiO_2 are transparent to the 1550 nm and 2000 nm wavelength, there is no absorption loss in the DBR. The reflectivity increases significantly with the increase of Si/SiO_2 pairs. Due to the large refractive index between Si and SiO_2, DBR with one pair of Si/SiO_2 (SOI substrate) can provide considerable reflectivity, but the transmission is high as well for the RCE structure. The DBR with 2 pairs of Si/SiO_2 (double SOI substrate) can provide greater than 90% free-space reflectivity over a wide band around 1550 nm and 2000 nm, which is sufficient for a high absorption efficiency. Though increasing N>4 will make the reflectivity of DBR approaches to 100%, the fabrication burden will increase as well. Therefore, 2 pairs of Si/SiO2 is the preferred choice considering both the efficiency and fabrication complexity.

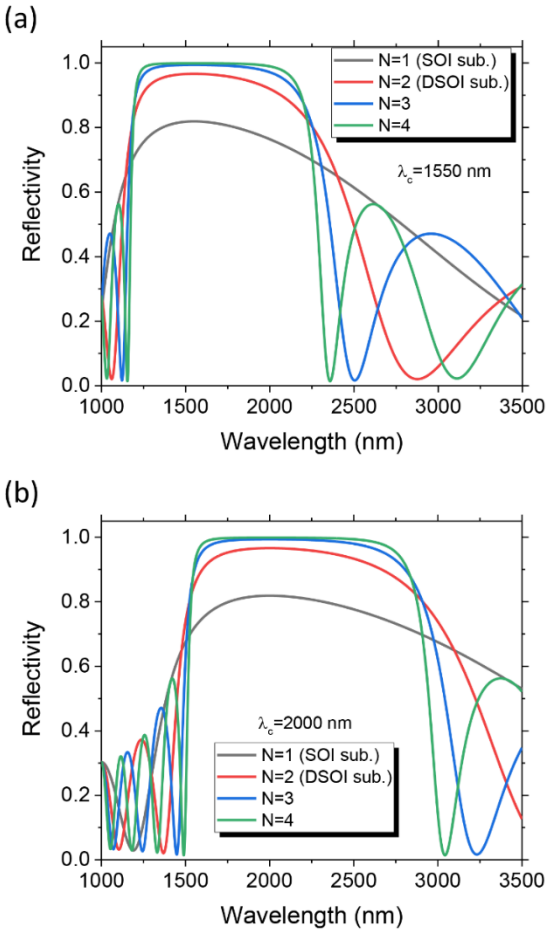

Fig. 3. Simulated reflectivity of Si/SiO_2 DBRs with (a) a thickness of 112 nm/269 nm for 1550 nm wavelength and (b) a thickness of 144nm/347nm for 2000 nm wavelength.

Fig. 4 shows the calculated absorption coefficient of $Ge_{1-x}Sn_x$ alloys with different Sn concentration for 1550 nm wavelength and 2000 nm wavelength at room temperature. It worth noting that the absorption coefficient of GeSn at both 1550 nm and 2000 nm wavelength can be enhanced by increasing Sn concentration. Therefore, GeSn, as the active absorption layer, has advantages over Ge at 1550 nm wavelength and is able to cover 2000 nm wavelength. In this work, the Sn concentration is tuned to achieve an absorption coefficient as large as 12500 cm^{-1}, which is comparable to conventional III-V absorption materials. Higher absorption coefficients can be achieved with higher Sn concentration. However, the lattice mismatch between GeSn and substrate will increase and growth temperature will decrease, resulting in the degradation of the material quality. Besides, the bandgap will shrink further. Both effects will increase the noise (DCR) of the SPAD considerably. Thus Sn concentrations x=3% and x=10% are chosen for 1550 nm wavelength and 2000 nm wavelength, respectively.

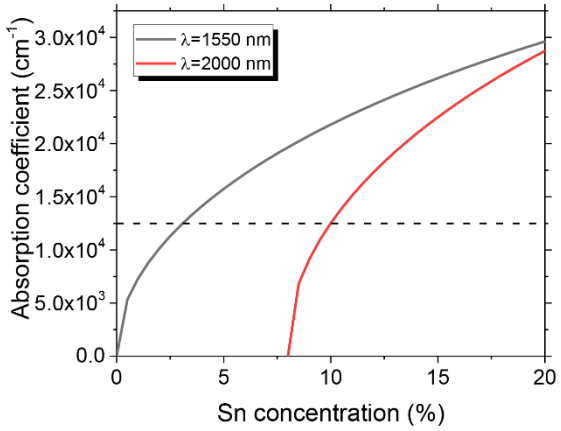

Fig. 4. Absorption coefficient of pseudomorphic GeSn on Ge as a function of Sn concentration for light wavelength of 1550 nm and 2000 nm, respectively. Dotted line represents an absorption coefficient of 12500 cm^{-1}.

Next, under the optimized DBR and Sn concentration, the thickness of GeSn layer is studied to obtain a resonance and achieve a high absorption efficiency at 1550 nm or 2000 nm. Based on equation 6, the absorption efficiency of $Ge_{0.96}Sn_{0.03}$ at 1550 nm and $Ge_{0.90}Sn_{0.10}$ at 2000 nm as a function of Sn concentration are simulated and shown in Fig. 5(a) and 5(b), respectively. The absorption efficiency of the RCE GeSn SPAD periodically increases as the GeSn thickness increases which is due to the resonance in the optical cavity. For 1550 nm band, with a GeSn thickness of 423 nm, the theoretical absorption efficiency tends to saturate (~97%) for RCE GeSn SPAD and only 25% for the same thickness of GeSn without a cavity. Absorption at 2000 nm shows a similar high absorption efficiency. With a GeSn thickness of 368 nm, the theoretical absorption efficiency at 2000 nm is 97% for RCE GeSn and only 22% for the same thickness of GeSn without a cavity. The absorption efficiency of RCE GeSn structures is 4~5 times of that of GeSn without a cavity which will benefit the SPDE enhancement of SPAD. It is attractive that the GeSn RCE structure without top DBR reflector could achieve such high absorption efficiency. In the following study, the optimized GeSn thicknesses are used for further analysis.

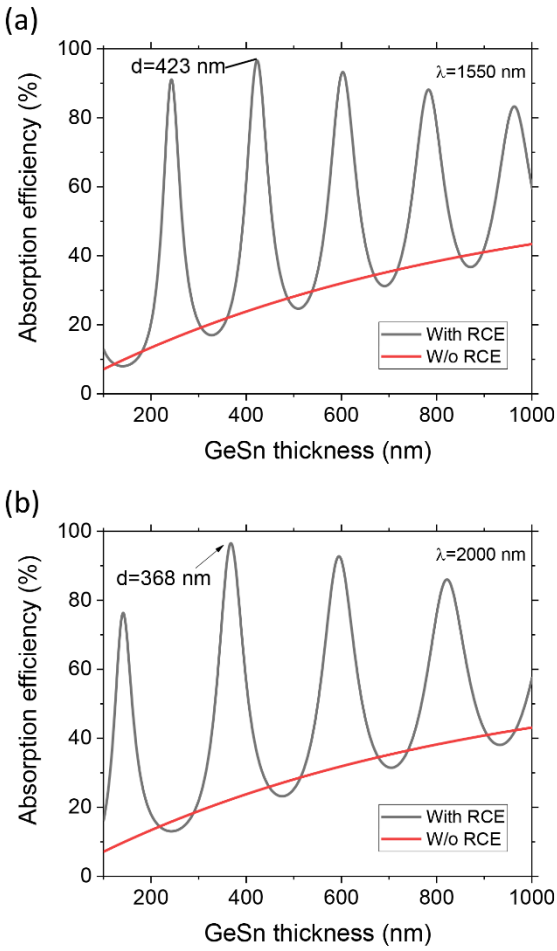

Fig. 5. (a) Absorption efficiency of RCE $Ge_{0.97}Sn_{0.03}$ SPAD and reference structure (same structure without DBR) as a function of the GeSn thickness at the wavelength of 1550 nm. (b) Absorption efficiency of RCE $Ge_{0.90}Sn_{0.10}$ SPAD and reference structure as a function of the GeSn thickness at the wavelength of 2000 nm.

B. Electrical characteristics and single-photon performance of RCE GeSn SPAD

The simulated electrical characteristics and avalanche triggering probabilities of the RCE GeSn SPADs with 10 μm diameters are shown in Fig. 6. Firstly, the dark current density versus the reverse voltage (*J-V*) characteristic of GeSn SPAD operating at room temperature is simulated and shown in Fig. 6(a). Ge SPAD is also simulated as a reference device. Due to the lack of the ionization coefficient values for GeSn, impact ionization coefficients of Ge are used. The carrier lifetime $\tau_n = \tau_p = 0.2$ ns of GeSn are used in this simulation. The *J-V* curves indicate avalanche effects of the SPADs with a breakdown voltage of 36 V. The punch-through voltage, which is the voltage at which the electric field penetrates into the GeSn absorption layer resulting in an efficient collection of photo-carriers, is estimated to be ~23 V. Both breakdown voltage and punch-through voltage are almost the same for GeSn SPAD with different Sn concentrations. The dark current density of Ge SPAD is ~1.3 A/cm^2 for 90% of the breakdown voltage. The value is comparable to the results of reported Ge APDs [38].

The dark current density of GeSn SPADs, especially biased above punch through voltage, increases due to the increased intrinsic carrier densities of GeSn by bandgap shrinkage. This result is consistent with reported GeSn/Si APDs [39].

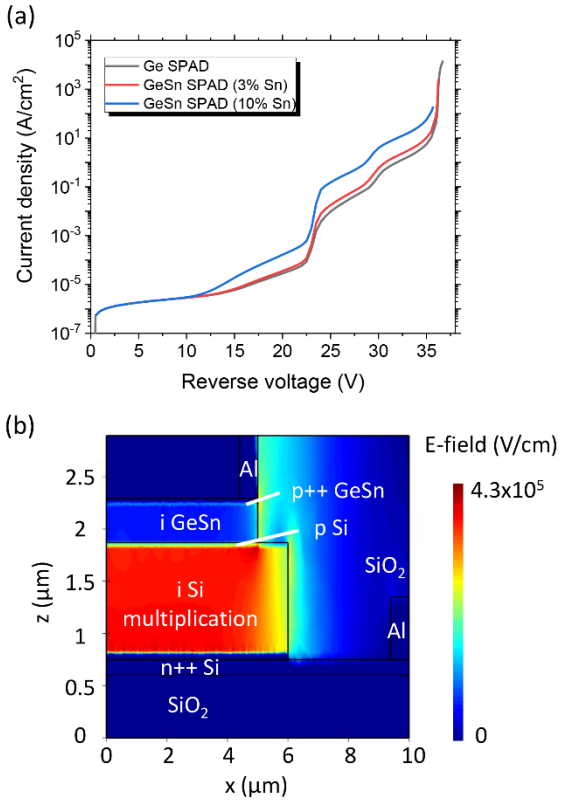

Fig. 6. (a) Dark current density versus the reverse voltage (*J-V*) of GeSn and Ge SPADs at room temperature. (b) 2D Electric field distribution in the RCE $Ge_{0.97}Sn_{0.03}$ SPAD for a reverse voltage of 39 V.

Fig. 6(b) shows the simulated 2D spatial electric field distribution of SPAD for a reverse voltage of 39 V (3 V above the breakdown voltage). The electric field satisfies the two design considerations: (1) The high and homogeneous electric field is confined in the Si multiplication layer; (2) a moderate electric field in GeSn absorption layer to drift photo-carriers into the multiplication layer. Fig. 7 shows the 1D electric field distribution (black solid line) as well as triggering probabilities (red solid and dashed lines) of electrons and holes along z-coordinate across the center of the SPAD with 3 V excess voltage above breakdown voltage at room temperature. It is worth noting that the maximum value of the electric field in the Si multiplication layer is lower than $7x10^5$ V/cm, which makes the contribution of BTBT for DCR negligible. The electric field in GeSn absorption layer is ~$5x10^4$ V/cm, which makes photo-generated carriers drifted at a saturation velocity and can be injected into the Si multiplication layer effectively before recombination. The SPAD employed in this work is an electron-avalanche SACM structure, which means only photo-generated electrons will drift into the multiplication layer and contribute to the SPDE. Therefore, the triggering probability of electrons P_e is more interesting for the design, as shown in the red solid line in Fig. 7. The electron triggering probability P_e, as expected, is 0 at the bottom of Si multiplication layer and increases to a maximum value of 0.66 at the bottom of the GeSn absorption layer due to the high electric field in the Si multiplication layer. P_e keeps unchanged in the GeSn layer due to the relatively low electric field within it.

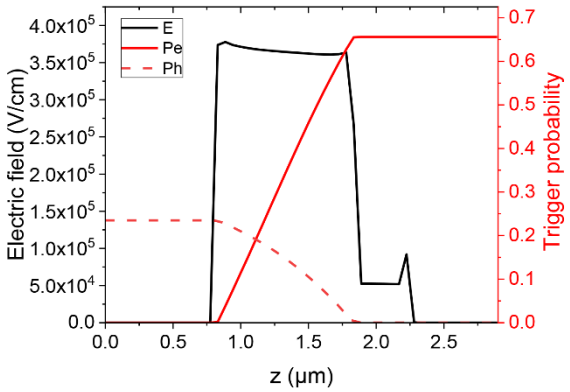

Fig. 7. Electric field distribution, triggering probabilities of electrons and holes along z-coordinate across the center of the SPAD with 3 V excess voltage above breakdown voltage at room temperature.

Next, the figures of merit for single-photon detection including SPDE, DCR and NEP are simulated as a function of excess bias voltage above breakdown voltage at room temperature, for different TDD values. The performances of the $Ge_{0.97}Sn_{0.03}$ SPAD for photons with 0.8 eV energy ($\lambda = 1550\ nm$) are shown in Fig. 8. When the excess bias voltage is 0 (Reverse voltage = 36 V), the triggering probability is 0, which means carriers can not trigger any avalanche events, resulting in no response to a single photon and the SPDE is 0. The result also indicates that the electrical simulation predicts an accurate breakdown voltage. As the excess bias voltage increases to 5 V, the SPDE reaches a value of 79%. The high value of the SPDE is due to the high absorption efficiency and high avalanche triggering probability of the RCE structure. Since the absorption efficiency does not limit the SPDE, the SPDE of RCE SPAD mainly depends on the triggering probability which can be controlled by reverse excess voltages. Therefore, the proposed SPAD with such high SPDE is interesting for some emerging quantum applications demanding a high SPDE, such as linear optical quantum computing (needs > 67% SPDE [40]).

Unfortunately, the DCR also increases as excess bias voltage increases (Fig. 8(b)). The straightforward way to decrease the DCR is to cool SPADs to suppress the thermally generated carriers. However, considering SPAD without an extra cooling system is more preferred in practical applications, DCR improved by the engineering of material quality of GeSn in terms of TDD is the better routine. Except extremely defective GeSn layers (TDD>$1x10^{12}$ cm^{-2}) [41], most reported TDD values of GeSn on Si substrates are in the order from 10^6 to 10^9 cm^{-2} [39], [42]–[47] Therefore, TDD-dependent DCRs of $Ge_{0.97}Sn_{0.03}$ SPADs with different excess voltages are simulated (Fig. 8(b)). According to the simulation, when the TDD decreases from $1x10^{10}$ to $1x10^6$ cm^{-2}, the DCR reduces 4 orders of magnitude. As a consequence, NEP decreases 2 orders of magnitude as well (Fig. 8(c)). Besides, different from DCR, NEP improves further as excess bias increases due to the significant enhancement of SPDE. The lowest NEP of the SPAD at room temperature from the simulation is ~$3x10^{15}$

W/Hz$^{1/2}$.

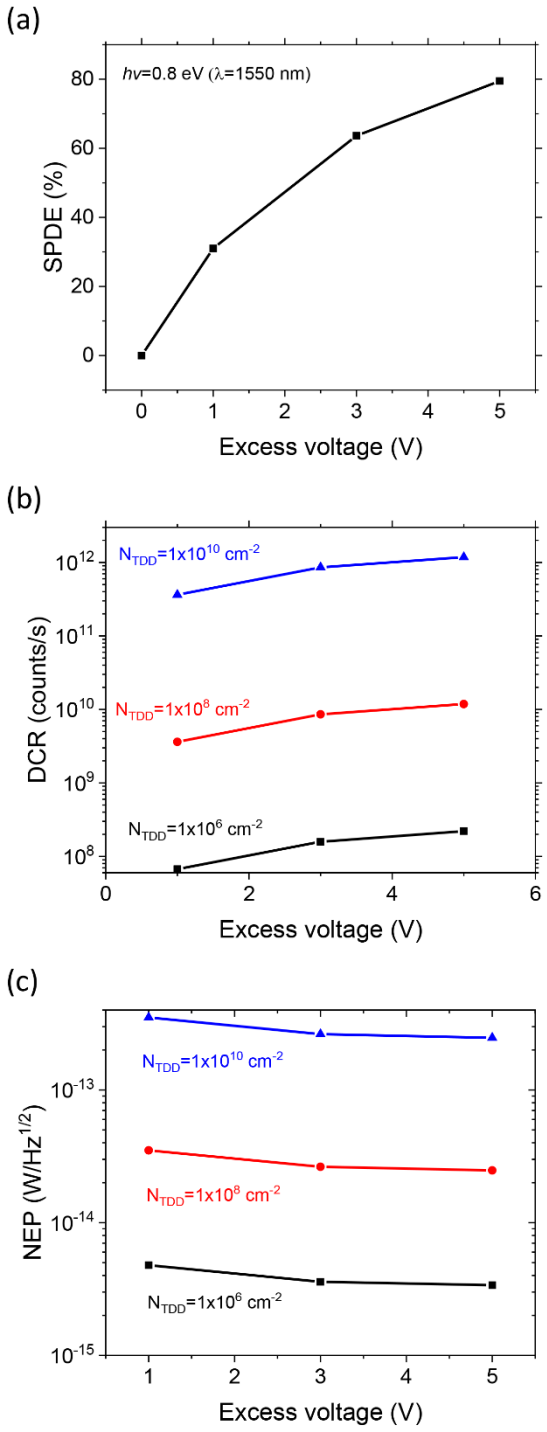

Fig. 8. (a) Calculated SPDE as a function of excess voltage at 1550 nm. Calculated (b) DCR and (c) NEP as a function of the excess voltage for different TDD values at room temperature at 1550 nm wavelength.

The performances of the RCE $Ge_{0.90}Sn_{0.10}$ SPAD for photons with 0.62 eV energy ($\lambda = 2000\,nm$) are shown in Fig. 9. Different from Ge SPAD that the SPDE will decrease dramatically for longer wavelength detection, RCE GeSn SPAD can maintain a high SPDE even the detection wavelength is extended from 1550 nm to 2000 nm. As shown in Fig. 9(a), with an excess bias voltage of 5 V, the SPDE is as high as 80%. However, GeSn SPAD for 2000 nm wavelength suffers from higher DCR than GeSn SPAD for 1550 nm even with the same level of TDD (Fig. 9(b)). Better material quality control or smaller device dimensions will help to keep the DCR of GeSn SPAD for 2000 nm wavelength to a relatively low level.

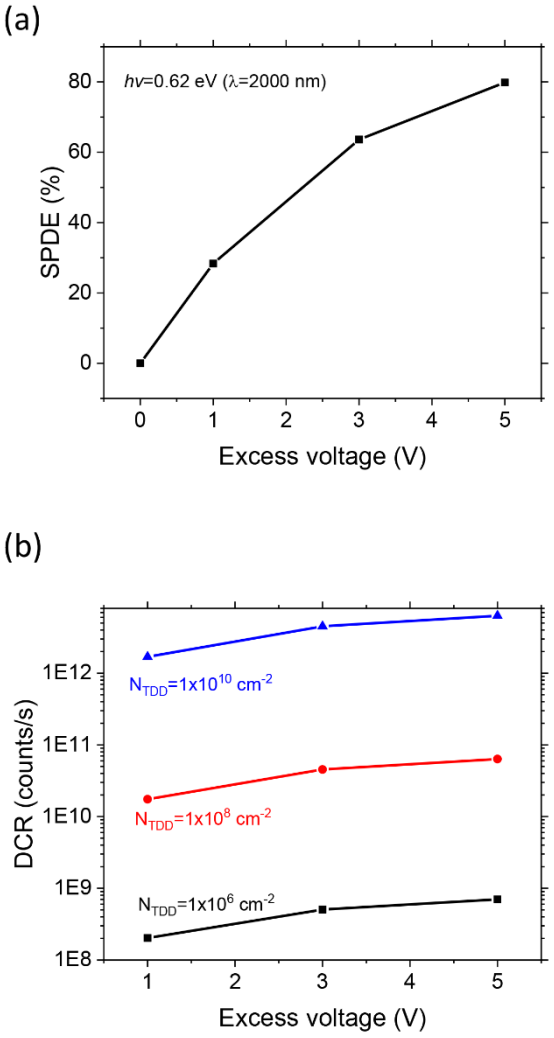

Fig. 9. (a) Calculated SPDE as a function of excess voltage at 2000 nm. (b) Calculated DCR as a function of the excess voltage for different TDD values at room temperature at 2000 nm wavelength.

Finally, it is interesting to compare the proposed RCE GeSn SPAD with the reported results of Ge SPADs (Table II). The most reported Ge SPAD demonstrates relatively poor SPDE (4~14%) at 1310 nm wavelength at low operation temperature (80~200 K) with a thick Ge layer (1 μm). The state-of-the-art planar Ge SPAD shows a maximum SPDE of 38% at 1310 nm wavelength at 125 K, representing a significant improvement in the performance. However, the SPDE of the planar Ge SPAD drops significantly to 0.5% at 1550 nm telecom wavelength due to the low absorption coefficient (460 cm^{-1} at 1550 nm wavelength). For the proposed RCE GeSn SPAD, due to the introduction of Sn and the cavity enhancement effect, the device could cover the detection wavelength to 2000 nm effectively with a thin absorber layer. Besides, by engineering the substrate to a low TDD level, the device could operate near room temperature with a similar DCR level to that of Ge SPAD operating at low temperatures.

TABLE II
COMPARISON BETWEEN PROPOSED RCE GESN SPAD AND REPORTED GE SPAD AT SWIR WAVELENGTH.

Structure	SPDE @ λ (nm)	DCR (Hz)	Operation T (K)	Diameter (μm)	Absorber thickness (nm)
Mesa Ge/Si SPAD [22]	14% @ 1310	10^8~10^9	200 K	30	1000
Mesa Ge/Si SPAD [21]	4% @ 1310	10^6~10^7	100 K	25	1000
Waveguide Ge/Si SPAD [12]	5.27% @ 1310	10^5	80 K	NA	NA
Planar Ge/Si SPAD [13]	38% @ 1310; 0.5% @ 1550	10^6~10^7	125 K	100~200	1000
RCE GeSn/Si SPAD	~80% @1550-2000	~10^7	300 K	10	320

V. CONCLUSIONS

In conclusion, a novel RCE GeSn SPAD detector is proposed and optimized for high-efficiency single-photon detection at 1,550 and 2,000 nm wavelength at room temperature for sensing and optical quantum applications. The corresponding fabrication methods based on direct epitaxy and wafer bonding are proposed as well. The results show that high photon absorption efficiency can be achieved by careful design of DBR reflectors, Sn concentration and GeSn thickness. High avalanche triggering probabilities can be achieved with proper doping concentrations of charge sheet layer and multiplication layer thickness. High absorption efficiency and high triggering probability lead to a high SPDE of ~80%, which is interesting for some emerging quantum applications demanding high SPDE, such as linear optical quantum computing. The effects of the TDD on the DCR and NEP are examined as well. The investigation demonstrates that the device could operate near room temperature with a similar DCR level to that of Ge SPAD operating at low temperatures by engineering the substrate to a low TDD level. A NEP of ~3×10^{15} W/Hz$^{1/2}$ is observed from RCE $Ge_{0.97}Sn_{0.03}$ SPAD for 1,550 nm wavelength at room temperature. This work shows that the proposed RCE GeSn SPADs are promising for high-efficiency single-photon detection in SWIR regime for sensing and optical quantum applications

ACKNOWLEDGMENT

This research project is supported by the National Research Foundation, Singapore, under its Competitive Research Program (CRP Award NRF-CRP19-2017-01), and Ministry of Education Tier-1 Project under Grant 2019-T1-002-040.

REFERENCES

[1] J. L. O'Brien, A. Furusawa, and J. Vučković, "Photonic quantum technologies," *Nat. Photonics*, vol. 3, no. 12, pp. 687–695, Dec. 2009.

[2] K. J. Gordon, V. Fernandez, P. D. Townsend, and G. S. Buller, "A short wavelength GigaHertz clocked fiber-optic quantum key distribution system," *IEEE J. Quantum Electron.*, vol. 40, no. 7, pp. 900–908, Jul. 2004.

[3] C. J. Pugh *et al.*, "Airborne demonstration of a quantum key distribution receiver payload," *Quantum Sci. Technol.*, vol. 2, no. 2, p. 024009, Jun. 2017.

[4] G. Buller and A. Wallace, "Ranging and Three-Dimensional Imaging Using Time-Correlated Single-Photon Counting and Point-by-Point Acquisition," *IEEE J. Sel. Top. Quantum Electron.*, vol. 13, no. 4, pp. 1006–1015, 2007.

[5] H. A. R. Homulle *et al.*, "Compact solid-state CMOS single-photon detector array for in vivo NIR fluorescence lifetime oncology measurements," *Biomed. Opt. Express*, vol. 7, no. 5, p. 1797, May 2016.

[6] D. Rosenberg, A. Lita, A. Miller, and S. Nam, "Noise-free high-efficiency photon-number-resolving detectors," *Phys. Rev. A*, vol. 71, no. 6, p. 061803, Jun. 2005.

[7] G. N. Gol'tsman *et al.*, "Picosecond superconducting single-photon optical detector," *Appl. Phys. Lett.*, vol. 79, no. 6, pp. 705–707, Aug. 2001.

[8] A. Peacock *et al.*, "Single optical photon detection with a superconducting tunnel junction," *Nature*, vol. 381, no. 6578, pp. 135–137, May 1996.

[9] R. E. Warburton, M. Itzler, and G. S. Buller, "Free-running, room temperature operation of an InGaAs/InP single-photon avalanche diode," *Appl. Phys. Lett.*, vol. 94, no. 7, p. 071116, Feb. 2009.

[10] Y. Liang, Y. Chen, Z. Huang, G. Bai, M. Yu, and H. Zeng, "Room-Temperature Single-Photon Detection With 1.5-GHz Gated InGaAs/InP Avalanche Photodiode," *IEEE Photonics Technol. Lett.*, vol. 29, no. 1, pp. 142–145, Jan. 2017.

[11] N. J. D. Martinez *et al.*, "Characterization of high performance waveguide-coupled linear mode avalanche photodiodes," in *2016 IEEE Optical Interconnects Conference (OI)*, 2016, vol. 24, no. 17, pp. 100–101.

[12] N. J. D. Martinez *et al.*, "Single photon detection in a waveguide-coupled Ge-on-Si lateral avalanche photodiode," *Opt. Express*, vol. 25, no. 14, p. 16130, Jul. 2017.

[13] P. Vines *et al.*, "High performance planar germanium-on-silicon single-photon avalanche diode detectors," *Nat. Commun.*, vol. 10, no. 1, p. 1086, Dec. 2019.

[14] R. Soref, "Group IV photonics: Enabling 2 μm communications," *Nat. Photonics*, vol. 9, no. 6, pp. 358–359, Jun. 2015.

[15] J. Meyer and I. Medfilms, "Laser Safety," *Am. J. Nurs.*, vol. 86, no. 8, p. 976, Aug. 1986.

[16] L. S. Rothman *et al.*, "The HITRAN 2004 molecular spectroscopic database," *J. Quant. Spectrosc. Radiat. Transf.*, vol. 96, no. 2, pp. 139–204, Dec. 2005.

[17] R. E. Bird and R. L. Hulstrom, "Additional solar spectral data sets," *Sol. Cells*, vol. 8, no. 1, pp. 85–95, Feb. 1983.

[18] A. M. Pawlikowska, A. Halimi, R. A. Lamb, and G. S.

Buller, “Single-photon three-dimensional imaging at up to 10 kilometers range,” *Opt. Express*, vol. 25, no. 10, p. 11919, May 2017.

[19] X. Ren *et al.*, “Time-of-flight Depth Imaging at 1550 nm Wavelength at Kilometer-range Distances Using an InGaAs/InP Single-Photon Avalanche Diode Detector,” in *CLEO: 2014*, 2014, vol. 21, no. 19, p. SM4E.8.

[20] B. Korzh *et al.*, “Provably secure and practical quantum key distribution over 307 km of optical fibre,” *Nat. Photonics*, vol. 9, no. 3, pp. 163–168, Mar. 2015.

[21] R. E. Warburton *et al.*, “Ge-on-Si Single-Photon Avalanche Diode Detectors: Design, Modeling, Fabrication, and Characterization at Wavelengths 1310 and 1550 nm,” *IEEE Trans. Electron Devices*, vol. 60, no. 11, pp. 3807–3813, Nov. 2013.

[22] Z. Lu, Y. Kang, C. Hu, Q. Zhou, H.-D. Liu, and J. C. Campbell, “Geiger-Mode Operation of Ge-on-Si Avalanche Photodiodes,” *IEEE J. Quantum Electron.*, vol. 47, no. 5, pp. 731–735, May 2011.

[23] M. K. Emsley, O. Dosunmu, and M. S. Unlu, “Silicon substrates with buried distributed Bragg reflectors for resonant cavity-enhanced optoelectronics,” *IEEE J. Sel. Top. Quantum Electron.*, vol. 8, no. 4, pp. 948–955, Jul. 2002.

[24] K. Y. Byun, I. Ferain, P. Fleming, M. Morris, M. Goorsky, and C. Colinge, “Low temperature germanium to silicon direct wafer bonding using free radical exposure,” *Appl. Phys. Lett.*, vol. 96, no. 10, p. 102110, Mar. 2010.

[25] M. R. M. Atalla *et al.*, “All-Group IV Transferable Membrane Mid-Infrared Photodetectors,” *Adv. Funct. Mater.*, vol. 2006329, p. 2006329, Oct. 2020.

[26] J. Zhang, M. A. Itzler, H. Zbinden, and J.-W. Pan, “Advances in InGaAs/InP single-photon detector systems for quantum communication,” *Light Sci. Appl.*, vol. 4, no. 5, pp. e286–e286, May 2015.

[27] M. S. Ünlü and S. Strite, “Resonant cavity enhanced photonic devices,” *J. Appl. Phys.*, vol. 78, no. 2, pp. 607–639, 1995.

[28] H. Tran *et al.*, “Systematic study of Ge 1−x Sn x absorption coefficient and refractive index for the device applications of Si-based optoelectronics,” *J. Appl. Phys.*, vol. 119, no. 10, p. 103106, Mar. 2016.

[29] W. G. Oldham, R. R. Samuelson, and P. Antognetti, “Triggering Phenomena in Avalanche Diodes,” *IEEE Trans. Electron Devices*, vol. 19, no. 9, pp. 1056–1060, 1972.

[30] Y. Xu, P. Xiang, X. Xie, and Y. Huang, “A new modeling and simulation method for important statistical performance prediction of single photon avalanche diode detectors,” *Semicond. Sci. Technol.*, vol. 31, no. 6, p. 065024, Jun. 2016.

[31] W. J. Kindt and H. W. Van Zeijl, “Modelling and fabrication of Geiger mode avalanche photodiodes,” *IEEE Trans. Nucl. Sci.*, vol. 45, no. 3, pp. 715–719, Jun. 1998.

[32] G. A. M. Hurkx, H. C. De Graaff, W. J. Kloosterman, and M. P. G. Knuvers, “A New Analytical Diode Model Including Tunneling and Avalanche Breakdown,” *IEEE Trans. Electron Devices*, vol. 39, no. 9, pp. 2090–2098, 1992.

[33] L. M. Giovane, H.-C. Luan, A. M. Agarwal, and L. C. Kimerling, “Correlation between leakage current density and threading dislocation density in SiGe p-i-n diodes grown on relaxed graded buffer layers,” *Appl. Phys. Lett.*, vol. 78, no. 4, pp. 541–543, Jan. 2001.

[34] B. Son, Y. Lin, K. H. Lee, Q. Chen, and C. S. Tan, “Dark current analysis of germanium-on-insulator vertical p-i-n photodetectors with varying threading dislocation density,” *J. Appl. Phys.*, vol. 127, no. 20, p. 203105, May 2020.

[35] G. A. M. Hurkx, D. B. M. Klaassen, and M. P. G. Knuvers, “A new recombination model for device simulation including tunneling,” *IEEE Trans. Electron Devices*, vol. 39, no. 2, pp. 331–338, 1992.

[36] J. G. Fossum and D. S. Lee, “A physical model for the dependence of carrier lifetime on doping density in nondegenerate silicon,” *Solid. State. Electron.*, vol. 25, no. 8, pp. 741–747, Aug. 1982.

[37] J. G. Fossum, “Computer-aided numerical analysis of silicon solar cells,” *Solid. State. Electron.*, vol. 19, no. 4, pp. 269–277, Apr. 1976.

[38] Z. Huang *et al.*, “25 Gbps low-voltage waveguide Si–Ge avalanche photodiode,” *Optica*, vol. 3, no. 8, p. 793, Aug. 2016.

[39] A. Mosleh *et al.*, “Investigation on the Formation and Propagation of Defects in GeSn Thin Films,” *ECS Trans.*, vol. 64, no. 6, pp. 895–901, Aug. 2014.

[40] M. Varnava, D. E. Browne, and T. Rudolph, “How Good Must Single Photon Sources and Detectors Be for Efficient Linear Optical Quantum Computation?,” *Phys. Rev. Lett.*, vol. 100, no. 6, p. 060502, Feb. 2008.

[41] S. Takeuchi, A. Sakai, K. Yamamoto, O. Nakatsuka, M. Ogawa, and S. Zaima, “Growth and structure evaluation of strain-relaxed Ge 1− x Sn x buffer layers grown on various types of substrates,” *Semicond. Sci. Technol.*, vol. 22, no. 1, pp. S231–S235, Jan. 2007.

[42] L. Zhang *et al.*, “Growth and Characterizations of GeSn Films with High Sn Composition by Chemical Vapor Deposition (CVD) Using Ge 2 H 6 and SnCl 4 for Mid-IR Applications,” *ECS Trans.*, vol. 98, no. 5, pp. 91–98, Sep. 2020.

[43] Y. Zhou *et al.*, “Optically Pumped GeSn Lasers Operating at 270 K with Broad Waveguide Structures on Si,” *ACS Photonics*, vol. 6, no. 6, pp. 1434–1441, Jun. 2019.

[44] T. Liu *et al.*, “Dislocation-related photoluminescence of GeSn films grown on Ge (001) substrates by molecular beam epitaxy,” *Semicond. Sci. Technol.*, vol. 33, no. 12, p. 125022, Dec. 2018.

[45] J. Zheng *et al.*, “GeSn p-i-n photodetectors with GeSn layer grown by magnetron sputtering epitaxy,” *Appl. Phys. Lett.*, vol. 108, no. 3, p. 033503, Jan. 2016.

[46] N. von den Driesch *et al.*, “Direct Bandgap Group IV Epitaxy on Si for Laser Applications,” *Chem. Mater.*, vol. 27, no. 13, pp. 4693–4702, Jul. 2015.

[47] S. Wirths *et al.*, “Lasing in direct-bandgap GeSn alloy grown on Si,” *Nat. Photonics*, vol. 9, no. 2, pp. 88–92,

Feb. 2015.